

# A Precise Carbon and Oxygen Abundance Determination in a Hot Jupiter Atmosphere

**Michael Line** (✉ [mrline@asu.edu](mailto:mrline@asu.edu))

Arizona State University <https://orcid.org/0000-0001-6247-8323>

**Matteo Brogi**

Warwick University

**Jacob Bean**

University of Chicago

**Siddharth Gandhi**

University of Warwick

**Joseph Zalesky**

Arizona State University

**Viven Parmentier**

University of Oxford

**Peter Smith**

Arizona State University

**Gregory Mace**

University of Texas-Austin

**Megan Mansfield**

University of Chicago

**Eliza Kempton**

University of Maryland <https://orcid.org/0000-0002-1337-9051>

**Jonathan Fortney**

University of California, Santa Cruz

**Evgenya Shkolnik**

Arizona State University

**Jennifer Patience**

Arizona State University

**Emily Rauscher**

University of Michigan <https://orcid.org/0000-0003-3963-9672>

**Jean-Michel Desert**

University of Amsterdam

**Jooost Wardenier**

University of Oxford

---

## Physical Sciences - Article

**Keywords:** Gas Giant Planets, Atmospheric Compositions, Giant Planet Formation, Ground-based Spectroscopy, Metallicity

**Posted Date:** June 9th, 2021

**DOI:** <https://doi.org/10.21203/rs.3.rs-593104/v1>

**License:**   This work is licensed under a Creative Commons Attribution 4.0 International License. [Read Full License](#)

---

**Version of Record:** A version of this preprint was published at Nature on October 27th, 2021. See the published version at <https://doi.org/10.1038/s41586-021-03912-6>.

# A Precise Carbon and Oxygen Abundance Determination in a Hot Jupiter Atmosphere

Michael R Line<sup>1,2</sup>, Matteo Brogi<sup>3,4,5</sup>, Jacob L. Bean<sup>6</sup>, Siddharth Gandhi<sup>3,4</sup>, Joseph Zalesky<sup>1</sup>, Vivien Parmentier<sup>7</sup>, Peter Smith<sup>1</sup>, Gregory N. Mace<sup>8</sup>, Megan Mansfield<sup>9</sup>, Eliza M.-R. Kempton<sup>10</sup>, Jonathan J. Fortney<sup>11</sup>, Evgenya Shkolnik<sup>1,2</sup>, Jennifer Patience<sup>1</sup>, Emily Rauscher<sup>12</sup>, Jean-Michel Désert<sup>13</sup>, & Joost P. Wardenier<sup>7</sup>

<sup>1</sup>*School of Earth and Space Exploration, Arizona State University, Tempe, AZ 85287, USA; mr-line@asu.edu*

<sup>2</sup>*NASA Astrobiology Institute, Virtual Planetary Laboratory Team, Seattle, Washington, USA*

<sup>3</sup>*Department of Physics, University of Warwick, Coventry CV4 7AL, UK*

<sup>4</sup>*Centre for Exoplanets and Habitability, University of Warwick, Coventry, UK*

<sup>5</sup>*INAF—Osservatorio Astrofisico di Torino, Turin, Italy*

<sup>6</sup>*Department of Astronomy and Astrophysics, University of Chicago, 5640 South Ellis Avenue, Chicago, IL 60637, USA*

<sup>7</sup>*Atmospheric, Oceanic, and Planetary Physics, Clarendon Laboratory, Department of Physics, University of Oxford, Oxford OX1 3PU, UK*

<sup>8</sup>*Department of Astronomy, University of Texas at Austin, 2515 Speedway, Austin, TX, USA*

<sup>9</sup>*Department of Geophysical Sciences, University of Chicago, 5734 S. Ellis Ave., Chicago, IL 60637*

<sup>10</sup>*Department of Astronomy, University of Maryland, 4296 Stadium Drive, College Park, MD 20742, USA*

<sup>11</sup>*Department of Astronomy and Astrophysics, University of California, Santa Cruz, CA 95064, USA*

<sup>12</sup>*Department of Astronomy, University of Michigan, 1085 South University Avenue, Ann Arbor, MI 48109, USA*

<sup>13</sup>*Anton Pannekoek Institute for Astronomy, University of Amsterdam, Science Park 904, 1098 XH Amsterdam, The Netherlands*

The origins of gas giant planets orbiting close to their host stars (“hot Jupiters”) remain a mystery despite more than a quarter-century of study<sup>1</sup>. The atmospheric compositions of these planets are highly sought after to provide insight to their formation location in protoplanetary disks, how they migrated to be so close to their host stars, and the relative role of solid versus gas accretion during their assembly<sup>2</sup>. However, simultaneous, bounded constraints on both carbon and oxygen abundances, which are key for understanding giant planet formation<sup>3,4,5,6</sup>, have been elusive<sup>7,8,9</sup>. Here, we report precise abundance measurements of both water and carbon monoxide in a hot Jupiter atmosphere via ground-based, high resolution spectroscopy. From these constraints on the primary carbon- and oxygen-bearing molecules, paired with upper limits on other minor volatile elemental carriers, we are able to derive the atmospheric elemental metal enrichment (metallicity) and the carbon-to-oxygen ratio (C/O). The inferred atmospheric metallicity is slightly sub-stellar ( $-0.48^{+0.15}_{-0.13}$ ) and the C/O is consistent with stellar ( $0.59 \pm 0.08$ ). The former is suggestive of a metal-

41 **depleted atmosphere relative to expectations based on extrapolation from the solar system,**  
42 **indicative of a greater partitioning of metals within the core vs the atmosphere. The C/O con-**  
43 **straint rules out gas-dominated accretion followed by disk free migration. Taken together in**  
44 **the context of past inferences, these results point to a diversity of planetary atmospheric**  
45 **compositions in addition to the observed diversity of planetary system architectures.**

46 We observed the day side hemisphere of the tidally-locked transiting hot Jupiter WASP-77Ab  
47 (1740 K, 1.21  $R_J$ , 1.76  $M_J$ , 1.36 day period<sup>10</sup>) for a single 4.7 hour continuous time-series se-  
48 quence on 14 December, 2020 with the Immersion GRating Infrared Spectrometer (IGRINS<sup>11</sup>)  
49 at the Gemini-South (GS) Observatory located on Cerro Pachón, Chile. Owing to the broad  
50 wavelength range (1.43 - 2.42  $\mu\text{m}$  over 54 spectral orders), high spectral resolution ( $R\sim 45,000$ ),  
51 and sensitivity ( $\text{SNR}\sim 180\text{-}270/\text{resolution-element}$ ), IGRINS on GS is particularly sensitive to the  
52 molecular lines from multiple carbon, nitrogen, oxygen, and sulfur bearing species (see Methods).  
53 Seventy-nine separate spectra (140 s/spectrum) were obtained during the pre-eclipse portion (Fig.  
54 1a) of the orbit when the hottest planetary hemisphere is present, covering a phase ( $\phi$ ) range be-  
55 tween 0.32 and 0.47 (where  $\phi=0$  is transit and 0.5 is occultation/secondary eclipse). The IGRINS  
56 Pipeline Package<sup>12</sup> is used for the basic data reduction, spectral extraction, and initial wavelength  
57 calibrations, with additional reduction steps described in the Methods. When observing from the  
58 ground, it is necessary to remove the contaminating effects of Earth’s atmosphere. Leveraging the  
59 rapidly changing Doppler shift of the planetary lines ( $\sim 140 \text{ km s}^{-1}$  over the observing window)  
60 compared to the relatively stationary telluric ( $0 \text{ km s}^{-1}$ ) and stellar lines ( $\sim 0.2 \text{ km s}^{-1}$ ), a principle  
61 component analysis (PCA, see methods) can be used to identify and remove the dominant time  
62 dependent contaminating sources<sup>13</sup>, leaving the planetary signal largely unscathed.

63 Removal of the telluric contamination also removes any continuum level information in the  
64 planet-to-star flux ratio<sup>14</sup>. In order to extract meaningful information from data processed in this  
65 way<sup>15,16</sup>, we must first cross-correlate (CC) the data with model templates. Using a set of represen-  
66 tative thermal emission models that include the dominant absorbers expected at these temperatures  
67 and over the IGRINS wavelength range (primarily,  $\text{H}_2\text{O}$  and  $\text{CO}$ ), we cross-correlate as a func-  
68 tion of velocity against each processed spectrum. Provided the model is an adequate template,  
69 the CC function (CCF) for each spectrum reaches its maximum at the planetary velocity (a sum  
70 of the system velocity and orbital velocity) at that specific orbital phase, and hence, trace out a  
71 CC trail in velocity<sup>17</sup>. The CC trail is clearly visible in Fig. 1b, corresponding to the appropri-  
72 ate planetary velocity components, demonstrating that we are detecting the planetary atmosphere  
73 as the planet orbits the star. We further leverage the circular orbital geometry, which predicts  
74 the phase-dependent line-of-sight velocity/Doppler shift, to determine the total atmospheric signal  
75 detection by summing over the CCF at each phase<sup>15,16</sup> (see Methods), for each pair of the plan-  
76 etary orbital velocity ( $K_p$ ) and system velocity ( $\Delta V_{sys}$ , relative to the reported literature value of  
77  $+1.685\pm 0.0004 \text{ km/s}$ ,<sup>10</sup>). Fig. 1c shows the total atmospheric thermal emission cross-correlation  
78 signal-to-noise, peaking at an  $\text{S/N}=12.8$  very near (offset by  $\sim -7 \text{ km s}^{-1} \Delta V_{sys}$ , see Methods) the  
79 anticipated pair of velocities, clearly indicating a strong detection of atmospheric thermal emission.

80 The next step is to identify the specific trace molecular species (the bulk atmosphere is pre-  
81 dominantly  $\text{H}_2/\text{He}$ ) present in the spectrum and retrieve their absolute abundances. To do this  
82 we perform an automated procedure via a Bayesian inference (retrieval) scheme<sup>14</sup>(see Meth-

83 ods). This approach simultaneously optimizes the volume mixing ratios for each trace species  
 84 ( $\log_{10}(n_i)$ ,  $i=\text{H}_2\text{O}$ , CO,  $\text{CH}_4$ ,  $\text{H}_2\text{S}$ ,  $\text{NH}_3$ , and HCN as well as a CO isotopic abundance parameter,  
 85  $\log_{10}({}^{13}\text{C}^{16}\text{O}/{}^{12}\text{C}^{16}\text{O})$  where  ${}^{12}\text{C}^{16}\text{O}$  is the main isotopologue—see Methods), the vertical temper-  
 86 ature structure, the planetary orbital and system velocities, and nuisance parameters to account for  
 87 uncertainties in the reported transit timing and possible signal stretching due the PCA analysis (see  
 88 Methods). This method accounts for all of the degeneracies that arise amongst the the multiple  
 89 overlapping molecular lines and absorption strength with atmospheric temperature gradient and  
 90 permits for absolute molecular abundance determinations<sup>14,18</sup>.

91 We achieve bounded constraints for  $\log(n_{\text{H}_2\text{O}})$  and  $\log(n_{\text{CO}})$  (Fig. 2a) and only upper limits  
 92 for the other species (see Methods), consistent with atmospheric chemical composition predictions  
 93 under typical ( $\sim$ solar elemental composition, thermochemical equilibrium) assumptions<sup>19</sup> (Fig.  
 94 1c). We are also able to retrieve a bounded constraint on the CO isotopic abundance ratio (see  
 95 Methods for a discussion). To quantify the significance of each species, we perform a nested model  
 96 comparison via a Bayes factor analysis<sup>20</sup> whereby each individual gas is removed and the retrieval  
 97 is re-run to compute<sup>21</sup> and compare the model evidences. The resulting log-Bayes factors amongst  
 98 the nested models are 298.2 for  $\text{H}_2\text{O}$  (strongly preferred), 55.6 for CO (strongly preferred), -1.8  
 99 (not preferred, see Methods) for the combination of  $\text{CH}_4+\text{H}_2\text{S}+\text{NH}_3+\text{HCN}$ , and 3.0 (moderately  
 100 preferred) for the  ${}^{13}\text{C}$  isotope. This quantification of individual species detection is different than  
 101 the classic<sup>22,23</sup> frequentist gas detection methods (see Methods) that compare the on-peak CCF  
 102 (nominal  $K_p$ ,  $\Delta V_{\text{sys}}$ ) to an off-peak region. We prefer the former as it fully incorporates the  
 103 change in likelihood and prior volume that arises from the removal of a gas, whereas the latter  
 104 is only relevant to a specific model choice out of an ensemble of possible models. These data  
 105 also prefer a monotonically decreasing relatively cool temperature profile (Fig. 2d), suggestive of  
 106 an atmosphere that either has a fairly efficient day-to-night atmospheric circulation (the predicted  
 107 day-side temperature for poor circulation planets should follow the hotter inverted predicted profile  
 108 in Fig. 2d) or lacks high altitude UV/optical absorbers (e.g., metal hydrides and oxides), possibly  
 109 indicative of night-side condensation (cold-trapping) of refractory species<sup>24</sup>.

110 The intrinsic elemental abundances in a planetary atmosphere are illuminating quantities be-  
 111 cause they are diagnostic of both atmospheric chemical processes (e.g., droplet condensation and  
 112 sedimentation) and formation conditions. Furthermore, C and O account for  $\sim 70\%$ <sup>25</sup> of the total  
 113 “metals” (e.g., any species heavier than H, He) in a typical solar-like composition gas, and are  
 114 hence, good tracers for the metal enrichment of an atmosphere. Since  $\text{H}_2\text{O}$  and CO are the domi-  
 115 nant C and O bearing molecules in this atmosphere (with relatively low abundance upper limits on  
 116 the other major C and O bearing molecules—see Methods), are expected to be largely unperturbed  
 117 by disequilibrium chemistry mechanisms at these temperatures<sup>19</sup>, and are expected to be homoge-  
 118 neous with altitude over the pressures probed by typical observations<sup>19</sup> (Fig. 2c), we can convert  
 119 them directly into the elemental oxygen ( $n_{\text{O}} = n_{\text{CO}}+n_{\text{H}_2\text{O}}$ ) and carbon ( $n_{\text{C}} = n_{\text{CO}}$ ) abundances.  
 120 It is customary to normalize the elemental abundances relative to hydrogen ( $n_i/n_{\text{H}}$ ), relative to  
 121 that in the sun ( $[\text{X}/\text{H}] := \log_{10}((n_{\text{X}}/n_{\text{H}})/(n_{\text{X}}/n_{\text{H}})_{\text{sun}})$ )<sup>25</sup> to facilitate comparisons with other as-  
 122 trophysical bodies in a common abundance reference frame. We find the elemental abundances in  
 123 the atmosphere of WASP-77Ab to be  $[\text{C}/\text{H}] = -0.46^{+0.17}_{-0.16}$ ,  $[\text{O}/\text{H}] = -0.49^{+0.14}_{-0.12}$ ,  $[(\text{C}+\text{O})/\text{H}] = -0.48^{+0.15}_{-0.13}$ ,  
 124 and a ratio of carbon to oxygen,  $\text{C}/\text{O} = 0.59 \pm 0.08$  (the Solar value is 0.55) (Fig. 2b). We also

125 retrieve a sub-terrestrial  $^{12}\text{C}/^{13}\text{C}$  abundance ratio (10.2-42.6 at 68% confidence, terrestrial value is  
126 89), but see methods for a discussion and interpretation of the CO isotopic abundance constraint.  
127 Fig. 3a summarizes the [C/H] and [O/H] compared to the solar system giant planets. At the  
128 unprecedented precision of these measurements, we can confidently determine that the C and O  
129 abundances are sub-solar/stellar (WASP-77A has been measured to have a solar [Fe/H],<sup>10</sup>) and fall  
130 below the solar system values, suggestive of different conditions for WASP-77Ab’s atmosphere  
131 formation than for our own solar system giants.

132 When and where a planet forms within the protoplanetary disk, the relative role of solid  
133 versus gas accretion, and chemical processing ultimately dictate the observed atmospheric com-  
134 positions, resulting in numerous potential outcomes for the elemental enrichment and abundance  
135 ratios. From the plethora of planet formation models, a few broad predictions have emerged for  
136 Jovian planet ( $M > 0.3M_J$ ) atmosphere compositions<sup>2</sup>: (i) Formation beyond the major ice lines  
137 ( $\text{H}_2\text{O}$ , CO,  $\text{CO}_2$ ) and subsequent inwards migration after disk dissipation leads to elevated ( $> 0.8$ )  
138 C/O and relatively low metal enrichment<sup>3,5,26</sup>, (ii) Formation and migration *within* a disk results in  
139 substantial oxygen rich planetesimal pollution, resulting in low ( $< 0.5$ ) C/O, and elevated metal  
140 enrichment, with [X/H] decreasing with increasing planet mass<sup>4,26</sup>, and (iii) Pebble accretion and  
141 drift<sup>5,27</sup> can result in both high C/O and super-solar metallicities.

142 It is with the sheer numbers of exoplanets that we can quantitatively test specific formation-  
143 to-atmosphere hypotheses, though at this time WASP-77Ab stands alone with this level of C and O  
144 abundance precision. However by combining this single precise point with the solar system carbon  
145 abundances and water-based oxygen abundances from low resolution Hubble Space Telescope  
146 (HST) observations<sup>28</sup> we can glean some insight into the diversity of planet formation outcomes  
147 (Fig. 3b). The Solar system carbon abundances (black diamonds) follow a decreasing trend (dotted  
148 line) with increasing planet mass<sup>7</sup>. The low resolution HST-based oxygen abundances<sup>28</sup> show  
149 virtually no trend with mass but span  $\sim 0.03$ - $300\times$ Solar enrichments, though the precisions are  
150 coarse for most objects. The WASP-77Ab C and O abundances both fall below the solar/stellar  
151 composition line and below the trend line predicted by the solar system, along with a few other  
152 O-based hot Jupiter abundances. These relatively low overall enrichments and  $\sim$ solar C/O are not  
153 consistent with the above broad predictions—e.g.,  $\sim$ solar C/O but low metal enrichment. Instead, a  
154 possible formation scenario consistent with the measured abundances could be that the planetary  
155 core accreted its atmosphere interior to the major ice lines with O rich but C depleted gas (possibly  
156 due to sequestration into refractory grains), a relative lack of planetesimal bombardment, which  
157 would deliver both C and O, post atmosphere accretion, and little to no dissolution of the core  
158 metals into the atmosphere (Fig. 3b).

159 The challenge in connecting giant planet atmosphere compositions to their formation condi-  
160 tions is formidable. Over the past decades the planetary science community has made substantial  
161 progress on this front, starting with carbon and nitrogen abundances in the solar system planets,  
162 to order-of-magnitude oxygen abundance constraints in hot Jupiter atmospheres, a stringent upper  
163 limit on the Jovian oxygen abundance from JUNO<sup>29</sup>, to now the first precision carbon *and* oxygen  
164 abundance measurements in exoplanets, advancing theory with each new measurement paradigm.  
165 Improvement in our understanding of how atmospheres came to be and how they evolve will con-

166 tinue as we push towards higher precision abundance measurements of more targets from both  
167 ground- and space-based platforms, ultimately paving the way for understanding our own Solar  
168 system’s formation history in the galactic context.

169 **Acknowledgements** M.R.L, J.J.F, J.L.B, and P.S. acknowledge support from NASA XRP grant 80NSSC19K0293.  
170 M.R.L. and E.S. acknowledge support from the Nexus for Exoplanet System Science and NASA Astrobi-  
171 ology Institute Virtual Planetary Laboratory (No. 80NSSC18K0829). M.B. and S.G. acknowledge sup-  
172 port from the UK Science and Technology Facilities Council (STFC) research grant ST/S000631/1. J.Z.  
173 acknowledges support from the NASA FINESST grant 80NSSC19K1420. E.M.-R.K. & E.R. thank the  
174 Heising-Simons Foundation for support. J.P.W. acknowledges support from the Wolfson Harrison UK Re-  
175 search Council Physics Scholarship and the UK Science and Technology Facilities Council (STFC). This  
176 work used the Immersion Grating Infrared Spectrometer (IGRINS) that was developed under a collaboration  
177 between the University of Texas at Austin and the Korea Astronomy and Space Science Institute (KASI)  
178 with the financial support of the Mt. Cuba Astronomical Foundation, of the US National Science Foundation  
179 under grants AST-1229522 and AST-1702267, of the McDonald Observatory of the University of Texas at  
180 Austin, of the Korean GMT Project of KASI, and Gemini Observatory

181 **Data Availability** The raw PLP extracted IGRINS data files are made available at [Zenodo or Dropbox  
182 Link] and the processed data cubes (wavelength x phase x order) available at [Zenodo or Dropbox Link].  
183 The nominal retrieval output samples are available here [Zenodo or Dropbox Link]

184 **Code Availability** The IGRINS PLP used to perform the initial reduction and extraction by the instrument  
185 team is available at <https://github.com/igrins/plp>. The barycenter correction and planetary phase calculations  
186 were made using the `python astropy` library found here <https://www.astropy.org/>. Python Numpy  
187 specific tools are noted in the text (e.g., the SVD for the PCA). Finally, we make available a simplified  
188 end-to-end python2/GPU HRCCS retrieval code example available here [github link upon acceptance]

189 **Author Contributions** M.R.L conceived of the idea , performed the data analysis and modeling, and  
190 wrote the manuscript. J.Z. (PI) and M.R.L. wrote the original IGRINS proposal. M.B. provided guidance  
191 on the cross-correlation analysis and conceptual framework. J.L.B. provided guidance on the context of  
192 the results. S.G. performed an independent Bayesian analysis to confirm the result. G.N.M. ran the PLP  
193 pipeline and also assisted in the IGRINS specific observational setup. V.P., P.S., G.M., M.M., E.M.-R.K.,  
194 J.J.F., E.S., J.P., E.R., J.-M.D, J.P.W., and L.P. helped with the original proposal/and or provided valuable  
195 insight/comments on the manuscript or through discussions.

196 **Competing Interests** The authors declare that they have no competing financial interests.

197 **Correspondence** Correspondence and requests for materials should be addressed to M.R.L (email: mr-  
198 line@asu.edu).

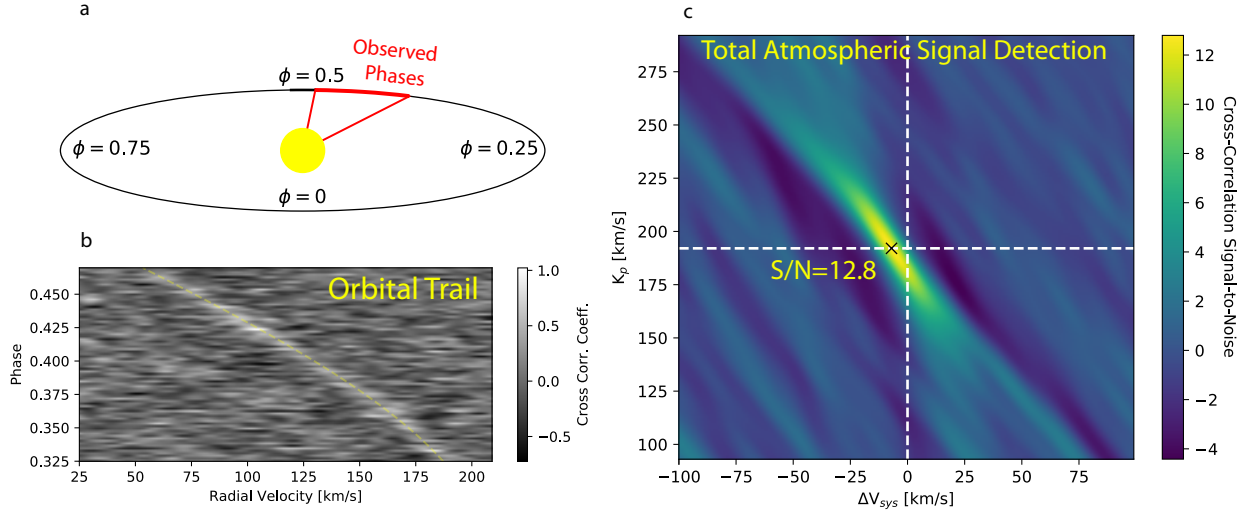


Fig 1: Summary of the planetary atmosphere signal detection. a) Illustration of the observed orbital phases (red), covering  $0.32 < \phi < 0.47$  (the orientation of the orbit is tilted for perspective). b) Cross correlation coefficient as a function of orbital phase/spectrum and planet velocity using a model template from the Bayesian inference procedure described in the text. The white trail corresponds to higher cross-correlation values (hence, atmospheric signal) and is consistent with the predicted velocity trail given the planetary orbital velocity and system velocity (light yellow dashed line). c) Atmospheric day-side thermal flux detection signal-to-noise (detection of absorption due to  $\text{H}_2\text{O}$  and  $\text{CO}$ , see text) as a function of the planetary orbital velocity,  $K_p$ , and the relative system velocity ( $\Delta V_{sys}$ ) (see Text). The significance was computed by subtracting off the mean of the cross-correlation map and then dividing through by the standard deviation of a box far from the planet velocity pair. White dashed lines indicate the known<sup>10</sup> velocities ( $K_p=192.06$ ,  $\Delta V_{sys}=0$   $\text{km s}^{-1}$ ) and the “ $\times$ ” denotes the location of the peak signal ( $S/N=12.8$ )

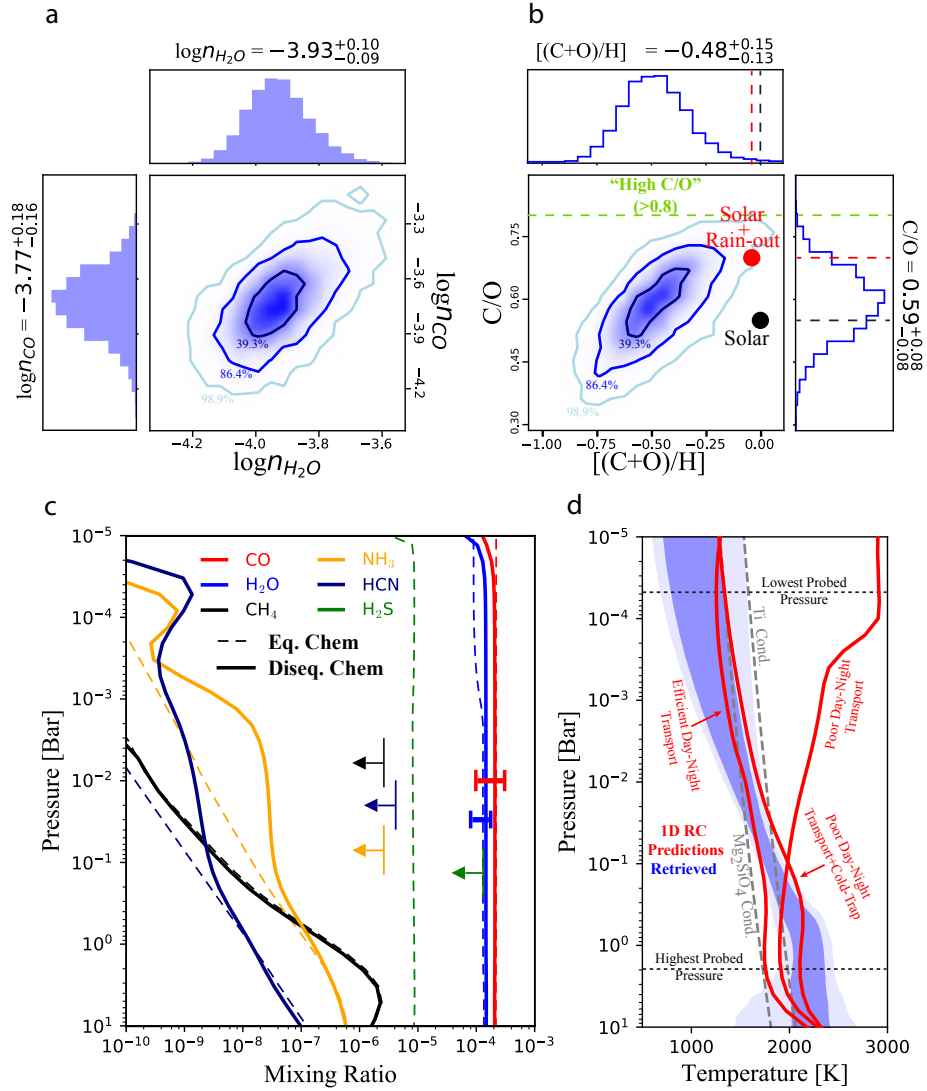


Fig 2: Summary of the composition and vertical thermal structure constraints, compared to predictions. a) marginalized and joint probability constraints for the  $\log_{10}$  volume mixing ratios ( $n$ ) of  $\text{H}_2\text{O}$  and  $\text{CO}$ . b) marginalized and joint probability constraints for the atmospheric C/O and metallicity proxy,  $[(\text{C}+\text{O})/\text{H}]$ . The solar abundance value<sup>25</sup> is given as the black point and the solar abundance value accounting for oxygen sequestration due to potential condensate rain out<sup>30</sup> on the night side<sup>24</sup> is shown as the red point. The 1(39.3%)- 2(86.4%)- and 3(98.9%) $\sigma$  joint probability contours are indicated in both a and b and the numerical values above each histogram are the marginalized median and 68% confidence interval range. c) Vertical abundance profiles for the major species predicted with both equilibrium (dashed) and disequilibrium (vertical transport and photochemistry, solid) chemistry (see Methods). d) Retrieved vertical temperature structure (magenta, 68 and 95% confidence intervals) compared to 1D radiative-convective equilibrium models with the coldest resulting from efficient day-to-night heat transport, the hottest poor heat transport, and the middle, poor heat transport but with nightside condensation of refractory species (see Methods).

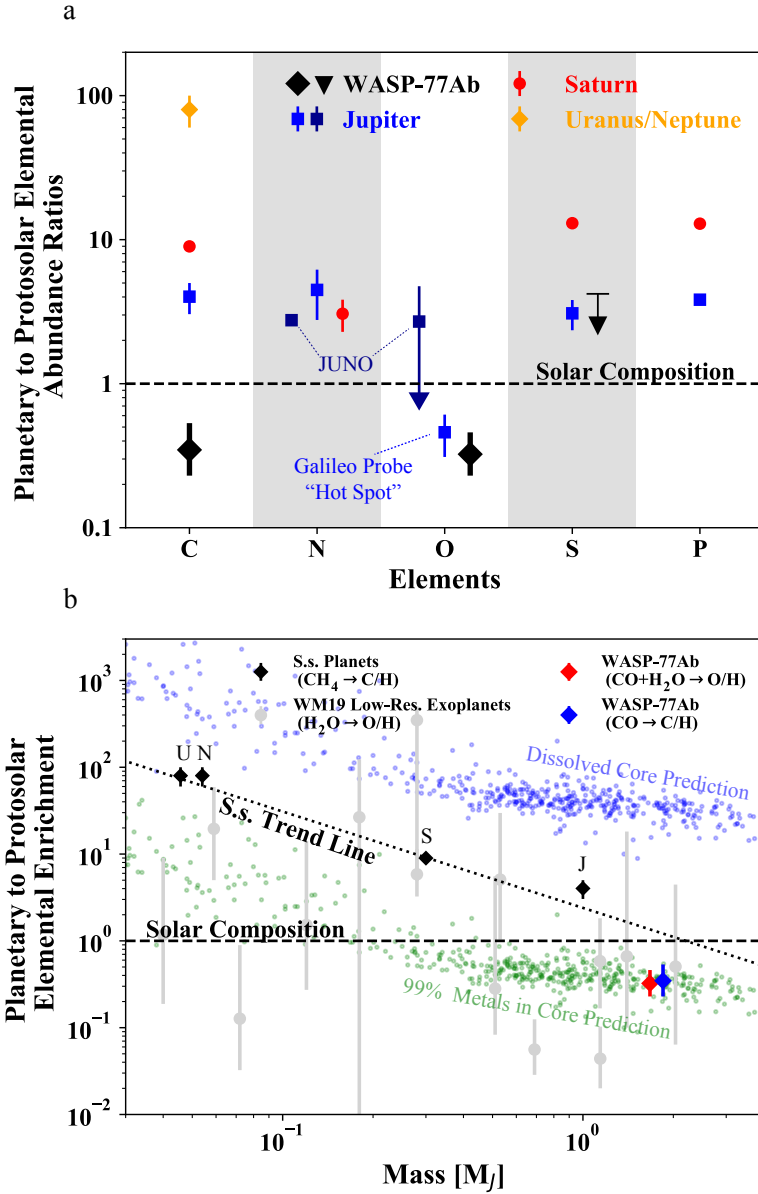


Fig 3: Comparison of the IGRINS WASP-77Ab abundance constraints with the solar system planets (a, adapted from<sup>31</sup>), with other exoplanets, and interior structure based envelope predictions (b). In (b), the gray points are from a uniform HST transmission spectrum water retrieval analysis by<sup>28</sup>. The solar system planets (black diamonds) follow a decreasing trend (dotted line) with increasing mass<sup>7,28</sup>. The light blue and green dots are the predicted envelope enrichments for the gas rich planet population based upon their mass and radius measurements<sup>32</sup>. The blue dots assume a coreless planet with all metals (e.g., C and O) uniformly mixed throughout the gas, whereas the green dots assume that 99% of the metals are in a solid planetary core (1% in the envelope).

# Methods

## 1 Observations & Data Analysis

We observed a 4.7 hour continuous pre-eclipse sequence of WASP-77Ab with IGRINS on Gemini South as part of program GS-2020B-Q-249 on Dec. 14 2020. A sequence of 79 A-B pairs (70 s each, or 140 s total per nod pair) covering a phase range ( $\phi$ ) between 0.325-0.47 achieving a per resolution-element signal-to-noise ratio of  $>200$  on average (ED Fig. 1). The WASP-77 system is composed of a primary, WASP-77A (G8V  $T_{eff}=5500\pm 80\text{K}$ ,  $M_K=8.4$ ) and a secondary WASP-77B (K5V,  $T_{eff}=4700\pm 200\text{K}$ ,  $M_K \sim 9.4$ ), separated by  $3.3''$ . To avoid contamination we adjusted the slit ( $0.3''$ ) position angle ( $150^\circ$ ) on WASP-77A to maximize the separation perpendicular to the slit ( $\sim 10$  slit widths away).

The IGRINS Pipeline Package (PLP)<sup>12,33</sup> is used to reduce, optimally extract the spectra, and perform wavelength calibrations. A further wavelength calibration fine adjustment is made by applying a linear stretch re-alignment of each spectrum with the spectrum at the end of the sequence. This ensures self-consistent alignment to enable more robust telluric detrending. Finally, due to heavy telluric contamination (median atmospheric transmittance  $<0.7$ ) we discard 11/54 orders near the edges of the H and K bands.

We use the Principle Component Analysis (PCA) method (singular value decomposition–SVD—with python’s `numpy.linalg.svd`) of telluric detrending as it requires little hand tuning and has worked well on other instruments<sup>13,22,34</sup>. The SVD is applied directly to each individual order by zeroing out the first  $N_{comp}$  eigenvalues that correspond to the dominant common mode-in-time (left singular values) components followed by a reconstruction of the “telluric free” data matrix. We remove 4 PC’s/SV’s for all orders. We experiment with between 2 and 14 and found little difference for values from 4 - 10 (below).

## 2 Modeling & Bayesian Inference Scheme

Rather than apply the standard cross-correlation analysis, we opt to use a Bayesian analysis/log-likelihood and modeling framework<sup>14</sup> so as to directly determine the atmospheric temperature/abundance constraints. We update our radiative transfer model<sup>14,35,36</sup> to include the latest line lists from EXOMOL<sup>37</sup> and HITEMP<sup>38</sup> –CH4:HITEMP<sup>39</sup>, CO:HITEMP<sup>40</sup>, NH3:aCeTY super-lines, H2S:AYT2<sup>41</sup>, HCN: Harris<sup>42</sup>, along with H<sub>2</sub>-H<sub>2</sub>/He collision induced absorption: HITRAN<sup>43</sup>. We include separately the <sup>12</sup>C<sup>16</sup>O and <sup>13</sup>C<sup>16</sup>O lines weighted by the built in terrestrial ratio of 1:89 (<sup>13</sup>C:<sup>12</sup>C) in the HITRAN/HITEMP line lists. When we refer to “CO” constraints in the main text, we refer to the main isotopologue, <sup>12</sup>C<sup>16</sup>O. Cross-sections are computed with the HELIOS-K package<sup>44,45</sup> at  $0.001\text{ cm}^{-1}$  resolution and a Voigt wing cut of  $100\text{ cm}^{-1}$  and then interpolated down to a constant  $R=250\text{K}$ . For water we use the POKOZATEL<sup>46</sup> line list with methods/broadening parameters described in<sup>47</sup>. ED Fig. 2 summarizes the opacity sources at a representative temperature/pressure.

The 1D atmosphere is parameterized with constant-with-altitude volume mixing ratios for the aforementioned gases (6 gases with He+H<sub>2</sub> as the remainder with  $n_{He}/n_{H_2}=0.176$ ) and the

237 6-parameter temperature profile scheme described in<sup>48</sup>. For completeness we also include as a free  
 238 parameter the CO isotopic abundance ratio,  $^{13}\text{C}^{16}\text{O}/^{12}\text{C}^{16}\text{O}$  ( $\log_{10}$  relative to the terrestrial value  
 239 of 1:89, more on this below). For HRCCS specific retrievals, we must also include the planet  
 240 Keplerian and system velocities ( $\Delta K_p$  and  $\Delta V_{sys}$  relative to the literature<sup>10</sup> reported values of  
 241  $192 \pm 11$  and  $1.6845 \pm 0.0004$  km s<sup>-1</sup>, respectively). Finally, we include as nuisance parameters  
 242 a stretching term to the planet flux to account for uncertainties in the reported planet/star radius  
 243 or data reduction induced stretching and a phase offset term to account for errors in the reported  
 244 ephemeris. Extended data Table 1 summarizes the parameters and their uniform prior ranges.

245 The model planet spectrum is convolved with both a planetary rotational ( $v \sin(i) = 4.52$  km/s)  
 246 and an instrumental broadening (assumed to be Gaussian) kernel followed by an interpolation  
 247 (using the python `scipy.interpolate.splrep/splev` functions) to the data wavelength  
 248 grid (accounting for the appropriate Doppler shift), and finally divided by a stellar model (either a  
 249 PHOENIX model or a blackbody) and scaled by the planet-to-star area ratio<sup>10</sup>.

250 Bayesian inference and model selection are performed using `pymultinest`<sup>21,49</sup> to eval-  
 251 uate the log-likelihood function<sup>14</sup>. The likelihood evaluation steps are the same as described in  
 252 ref.<sup>14</sup> except that we use the PCA instead of the airmass detrending method. To do so, we save  
 253 the  $N_{comp}$  discarded eigenvectors from the SVD to reconstruct the telluric/systematic data matrix  
 254 followed by a multiplicative injection of the model (Doppler shifted matrix of  $1 + (F_p/F_{star})(\lambda, \phi)$ ).  
 255 The PCA/SVD is then re-applied to the model injected data for each order. This matrix is then  
 256 cross-correlated, frame-by-frame, order-by-order, with the true data matrix and the log-likelihood  
 257 evaluated, for each model/parameter instance. A typical retrieval under this set-up (17 parameters,  
 258 500 live points) runs in about 3 days ( $\sim 270\text{K}$  likelihood evaluations) if utilizing 24 CPUs (for  
 259 paralleling–pythons’ `joblib` package—the model-injected data PCA computation for each order)  
 260 and a single NVIDIA Tesla V100 GPU for the radiative transfer.

### 261 3 Extended Results

262 **Retrieved Constraints** ED Fig. 3 summarizes the full posterior/parameter constraints and rep-  
 263 resentative best fit model (inset) and is from where the primary results (e.g., main text Fig. 2)  
 264 discussed in the main text are derived. The temperature profile confidence intervals presented in  
 265 main text Fig. 2d are reconstructed from random posterior draws<sup>50,51</sup>.

266 We also perform a Bayes factor model selection test<sup>52,53</sup> between the full model and the  
 267 full model less one gas to assess the justification of the inclusion of each gas as a free parameter.  
 268 Unsurprisingly, given the posterior constraints, we obtain strong detections for both water (log-  
 269 Bayes factor of 298.2, corresponding to a  $21.3\sigma$  detection<sup>52,53</sup>) and CO (log-Bayes factor of 55.6,  
 270 corresponding to a  $10.8\sigma$  detection), and a mild disfavoring of all other gases (log-Bayes factor  
 271 of -1.8). This is consistent with the stringent constraints on water and CO and the upper limits  
 272 (non-detections) of the other gases. We revisit the isotope in a later section.

273 There is a non-negligible offset ( $\sim 1.5\sigma$ , see  $dV_{sys}$  histogram in ED Fig. 3) in the relative  
 274 system velocity. Such offsets are not uncommon<sup>9,23,54</sup> and can arise for a variety of reasons includ-  
 275 ing uncertainties in the propagated mid-point timing during the event (e.g., the propagated eclipse

Table 1: Retrieved parameters and their prior range

Parameter	Description	Prior Range
$\log_{10} n_i$	log of the gas volume mixing ratios (i=H <sub>2</sub> O, CO, CH <sub>4</sub> , H <sub>2</sub> S, NH <sub>3</sub> , HCN)	-12 - 0
$[^{12}\text{CO}/^{13}\text{CO}]$	$\log_{10}$ isotopic ratio relative to terrestrial (89:1)	-3 - 3
T0	Top of Atmosphere Temperature [K]	500-2000
logP1	layer 1-2 boundary pressure [bar] (see Fig. 1 <sup>48</sup> )	-5.5 - 2.5
logP2	layer 2 knee pressure [bar] (see Fig. 1 <sup>48</sup> )	-5.5 - 2.5
logP3	isothermal layer pressure start [bar] (see Fig. 1 <sup>48</sup> )	-2 - 2
a1	upper atm. Temp. shape param. (see Eq. 2 <sup>48</sup> )	0.02 - 1
a2	middle atm. Temp. shape param. (see Eq. 2 <sup>48</sup> )	0.02 - 1
$dK_p$	Planet Orbital velocity relative to published [km/s]	-20 - 20
$dV_{sys}$	System velocity relative to published [km/s]	-20 - 20
log(a)	$\log_{10}$ planet flux scale factor	-1 - 1
$d\phi$	Orbital phase offset	-0.01 - 0.01

276 midpoint uncertainty is  $\sim 260$ s which would correspond to a  $\sim 2.7$  km/s velocity uncertainty at the  
 277 observed orbital phases), a small previously unnoticed eccentricity, or perhaps, more intriguingly  
 278 a combination of rotation ( $\sim 4.5$  km/s) which might preferentially blue shift a dayside hot spot  
 279 and/or longitudinal temperature advection (west-to-east winds,  $\sim 2$  km/s<sup>55</sup>). Whatever the source  
 280 of the velocity offset, it is inconsequential for the chemical and thermal profile constraints as it is  
 281 non-degenerate with those atmospheric parameters.

282 For legacy with past works we also include the “classic”<sup>15,16,22,23</sup> CCF analysis (ED Fig. 4)  
 283 about the maximum likelihood solution summarized with individual gas “detections” in the  $K_p$ -  
 284  $\Delta V_{sys}$  plane and slices along the systemic velocity axis at the literature reported  $K_p$  value. We also  
 285 include, for comparison purposes, these same data products in delta-log-likelihood space (right  
 286 column of ED Fig. 4). It is worth noting how the log-likelihood mapping boosts the signal of CO  
 287 by adding information about the line shape and amplitude relative to the continuum, which is what  
 288 ultimately enable absolute abundance constraints.

289 **Physical Plausibility Assessment** We assess the physical/chemical plausibility of the retrieved  
 290 quantities with a 1D radiative-convective-thermochemical-equilibrium<sup>56,57,58,59</sup> and a chemical ki-  
 291 netics -transport-photochemical solver<sup>60</sup>. These tools self-consistently predict the 1D temperature  
 292 profile and molecular abundances given the incident stellar flux (or scaling) and elemental abun-  
 293 dance inventory ([M/H]=-0.4, C/O=0.58).

294 The results of this exercise are shown in main text Figs. 2c,d. We explore several plausible  
 295 chemical/radiative scenarios: (i) “efficient day-night transport” which permits the planet to evenly  
 296 re-radiate over both the day-and-night hemispheres<sup>61</sup>, (ii) “poor day-night transport”, in which  
 297 the planet only re-radiates over the dayside hemisphere<sup>61</sup>, (iii) “poor day-night transport+cold  
 298 trap” which is the same as (ii) but removes UV-optical absorbing refractory opacities (TiO, VO,

299 FeH, CrH, MgH, etc.), to mimic loss due to nightside condensation and what would be nominally  
300 predicted<sup>62,63</sup>, and (iv) thermochemical equilibrium (“Eq. Chem”) vs. photochemical-transport  
301 kinetics (“Diseq. Chem”). The latter (chemistry in main text Fig. 2c) assumes the temperature  
302 profile from (i) for simplicity. The retrieved molecular abundances are consistent with the plausible  
303 chemistry (photochemistry/transport matter little as this is a hot planet). The retrieved temperature  
304 profile is consistent with both the cooler two temperature profile scenarios, suggesting either day-  
305 night-cold trapping and/or efficient day-to-night heat transport.

306 **Elemental Abundance Determinations & Interpretation** The chemical plausibility, dominance  
307 of CO and H<sub>2</sub>O, and uniformity with pressure/altitude permits us to directly compute the C and  
308 O enrichments and carbon-to-oxygen ratio (main text Fig. 1b). The total C abundance is given  
309 by CO/H, O by (H<sub>2</sub>O+CO)/H, and H by 2H<sub>2</sub> (where H<sub>2</sub>=0.837—the equilibrium chemistry value  
310 at WASP-77Ab temperatures). Solar abundances from<sup>25</sup> (C/H=2.95×10<sup>-4</sup>, O/H =5.37×10<sup>-4</sup>,  
311 C/O=0.55) are used when referencing the “relative to solar values” (e.g., main text Fig. 3) with  
312 “[ ]” referring to the log<sub>10</sub> relative to solar. This results in a [C/H]=-0.46±0.17 (0.24 - 0.51×Solar),  
313 [O/H]=-0.49±0.13, (0.24 - 0.44×Solar), [(C+O)/H]=-0.48±0.14 (0.24 - 0.46×Solar), and a C/O=  
314 0.59±0.08. [(C+O)/H] is used as a proxy for the total metal enrichment ([M/H]). We include as  
315 a reference in main text Fig. 2b the solar values (the black solar point) and the rain-out value  
316 (red point) whereby O is lost into refractory condensates (possibly on the nightside, assuming  
317 3.28 O atoms per Si atom from silicate cloud formation<sup>64</sup> results in a 22% reduction in O). If we  
318 “correct” for the loss of O due to condensate formation, then we obtain a [(C+O)/H]=-0.41±0.14  
319 (0.29 - 0.54×Solar) and C/O=0.46±0.08. We use the “non-rainout” abundances in the main-text  
320 discussion and Fig. 3.

321 The C and O abundances for WASP-77Ab are interpreted through the lens of the solar sys-  
322 tem abundance determinations, the representative exoplanet population abundances as measured  
323 with low spectral resolution platforms (e.g., HST), and theoretical models in main text Fig. 3.  
324 To compare to the solar system (main text Fig. 3b) we use the abundances given in Table 1 in<sup>65</sup>  
325 (from references therein), with recent updates from JUNO<sup>29</sup>. It is worth noting, however, that the  
326 reported JUNO value for O (based upon H<sub>2</sub>O via the microwave radiometer equatorial measure-  
327 ments), while seemingly greater than the Galileo Probe “hot spot” measurement, is technically  
328 not a bounded constraint, rather more of an upper limit (see Fig. 5b in ref.<sup>29</sup>). Thus it remains  
329 a mystery as to the true H<sub>2</sub>O/O abundance in Jupiter. Comparatively, our measurements provide  
330 bounded constraints on both C and O at sub-solar/stellar values.

331 Main text Fig. 3b places WASP-77Ab’s abundance determinations in the context of low res-  
332 olution HST H<sub>2</sub>O/O measurements<sup>28</sup> (gray points), the solar system CH<sub>4</sub>/C-based measurements  
333 (from Fig 3a) and trend line, and interior structure based envelope metallicity predictions<sup>32</sup> (blue,  
334 green dots) as a function of planetary mass. If all abundances scaled proportionally to the total  
335 envelope metallicity, and the population synthesis predictions from<sup>66</sup> and<sup>4</sup> were true, we would  
336 expect exoplanet atmosphere metal enrichment’s to loosely follow the solar system trend line (dot-  
337 ted). There is clearly no trend with the H<sub>2</sub>O based O measurements in<sup>28</sup> (see also<sup>67,68</sup>), though the  
338 uncertainties are quite large. This could be suggestive that perhaps O is “depleted” (e.g., via high  
339 C/O), though without a C measurement for each planet this cannot be confirmed. The precisely

340 constrained C and O in WASP-77Ab both fall well below the trend line, and even below solar  
341 composition.

342 Ref.<sup>32</sup> provide predictive models for the maximum metal enrichment (based upon O) for the  
343 exoplanet population given their measured mass and radius for a “core-less” planet, e.g., the metals  
344 and gas are well mixed throughout the entire planet. This is clearly extreme as these values (blue  
345 dots, main text Fig. 3b) vastly overshoot the measured Jupiter and Saturn envelope enrichment’s,  
346 suggesting a large fraction of metals must be sequestered into a solid core (on the order of 90%).  
347 To match the retrieved depletion for WASP-77Ab, approximately 99% of the accreted metals must  
348 be in the planetary core (assuming the observed atmospheric composition is representative of the  
349 entire envelope). One cannot tell the formation story with a single planet as the vast complexities  
350 between the composition of accreted gas and the partitioning of metals/solids within the core are  
351 not yet cleanly predictable. A larger survey of planets with precisions obtained here could shed  
352 light on this seemingly insurmountable problem.

#### 353 **4 A Series of Robustness Tests**

354 To test the robustness of the abundance and temperature profile constraints, we perform a battery  
355 of tests that explore the impact of data processing and modeling assumptions on the retrieved H<sub>2</sub>O,  
356 CO abundances, and temperature profile (summarized in ED Fig. 5).

357 The first test is used to evaluate the influence of the TP-profile parameterization (“Tempera-  
358 ture Profile Parameterization”, top histogram row, first TP-profile panel). The atmospheric param-  
359 eterization is identical to that described above, but replacing the parameterization from ref.<sup>48</sup> with  
360 the 3-parameter analytic prescription from refs.<sup>69,70</sup>. This has virtually no effect on the retrieved  
361 gas abundances, and a slight change in the temperature gradient in the  $\sim 1 - 0.01$  bar region.

362 The second test gauges the impact of spatial heterogeneity’s in temperature<sup>55,71</sup>. If the planet  
363 had strong spatially varying temperatures, like a dominating hot spot, we would expect to retrieve  
364 different temperatures between the first half and the second half of the observing sequence as  
365 the heterogeneities rotate into/out of view. To test this, we broke the observing sequence in half  
366 (compared to the full sequence) as if each were its own separate observation, each having 40  
367 (39) frames/spectra per sequence. The entire PCA analysis/retrieval procedure above was then  
368 applied to each half-sequence. For computational reasons we used the faster 3-parameter analytic  
369 TP-profile prescription from refs.<sup>69,70</sup> (since this choice did not matter in the first test). These  
370 results are shown (“3D Temperature Effects”) in the middle histogram row and middle TP-profile  
371 panel of ED Fig. 5. Again, this had little influence other than increasing the uncertainties on the  
372 abundances and TP-profile due to the reduced data set size per half-sequence. This suggests that a  
373 “1D” atmosphere/retrieval is sufficient in this case and does not result in any measurable bias.

374 The last sequence of tests explores somewhat random processing/model assumptions (“Pro-  
375 cessing Assumptions”, bottom histogram row, last TP-profile panel). The Reference (REF) model  
376 here assumes the 3-parameter analytic TP-profile prescription from refs.<sup>69,70</sup>, H<sub>2</sub>O and CO as  
377 the only abundance free parameters (as we only obtained upper limits on the others above), a  
378 PHOENIX stellar spectrum (for  $F_p/F_*$ ), a Gaussian instrumental profile consistent with R=45K,

379 no rotational broadening (it too does not matter), 4-principle components in the processing, and  
 380 R=250K model resolution (as in the main analysis). We explored these dimensions/assumptions  
 381 one-at-a-time by 1) changing the instrumental profile to that of an R=71K instrument (IP/71K,  
 382 narrower), 2) using a blackbody stellar spectrum (BB Star) instead of a PHOENIX model, 3) 8-  
 383 principle components removed in the PCA (8 PC), and R=500K model resolution (R=500K xsecs).  
 384 None of these assumptions had a significant influence on the retrieved H<sub>2</sub>O and CO abundances or  
 385 temperature profile.

386 Finally, we under go an independent Bayesian/retrieval analysis using an entirely indepen-  
 387 dent tool/code (HyDRA-H<sup>18,72</sup>), but also utilizing the log-likelihood mapping from<sup>14</sup> and PCA for  
 388 airmass detrending. A comparison of a subset of common parameters is shown in ED Fig. 6. In  
 389 this comparison, HyDRA-H retrieves for identically the same parameters as described in ED Table  
 390 1 with the following differences: the NH<sub>3</sub>, HCN, H<sub>2</sub>S, and CH<sub>4</sub> gas mixing ratios are not included  
 391 and no orbital phase offset parameter is included. The results sufficiently agree, with only a slight  
 392 (1.5  $\sigma$ ) offset in the median values of the retrieved CO abundance and small differences in the slope  
 393 of the TP-profile. We also note (not shown) that the retrieved velocities and scale factor are in very  
 394 good agreement as well. These differences don't affect our main conclusions that the overall C and  
 395 O enrichment is low, the C/O constraints rule out high C/O scenarios, and the temperature profile  
 396 decreases with decreasing pressure (e.g., no thermal inversion).

397 We thus conclude that the resulting constraints, and subsequent derivatives there-of, pre-  
 398 sented in the main text are resilient against the common data analysis choices and modeling as-  
 399 sumptions.

## 400 **5 A Potential <sup>13</sup>C<sup>16</sup>O/<sup>12</sup>C<sup>16</sup>O Constraint**

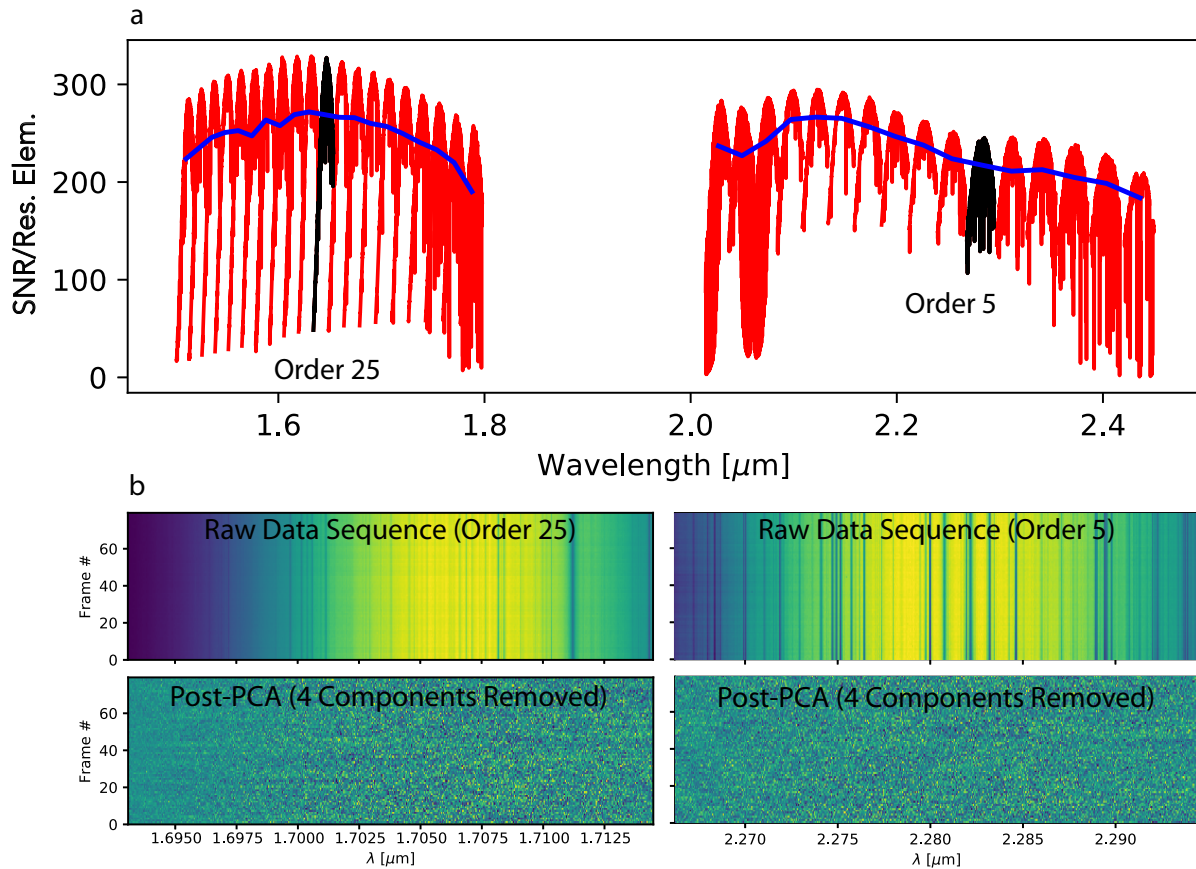
401 Isotopic abundance ratios provide an additional composition dimension<sup>65,73,74</sup> with which we can  
 402 explore planet formation and atmospheric chemistry due to their sensitive mass/temperature depen-  
 403 dent fractionation. High resolution observations are potentially sensitive<sup>75</sup> to isotopic abundance  
 404 ratios for select molecules, specifically, for IGRINS, those of CO-<sup>12</sup>C<sup>16</sup>O/<sup>13</sup>C<sup>16</sup>O (primarily near  
 405 the 2.3  $\mu$ m CO bandhead). For these reasons, we include this ratio as a free parameter (ED Table  
 406 1).

407 Surprisingly (ED Fig. 3), we obtain a bounded constraint with [<sup>12</sup>C<sup>16</sup>O/<sup>13</sup>C<sup>16</sup>O]=-0.65<sup>+0.33</sup><sub>-0.29</sub>  
 408 (0.11-0.48 $\times$ terrestrial, or <sup>12</sup>C<sup>16</sup>O/<sup>13</sup>C<sup>16</sup>O of 10.2 - 42.6 ). We perform a similar Bayes factor  
 409 analysis as above, but find only moderate detection (log-Bayes factor=3.0 or 2.9 $\sigma$ ). We do not see  
 410 any signature within the CCF itself, though this is not unexpected<sup>75</sup>.

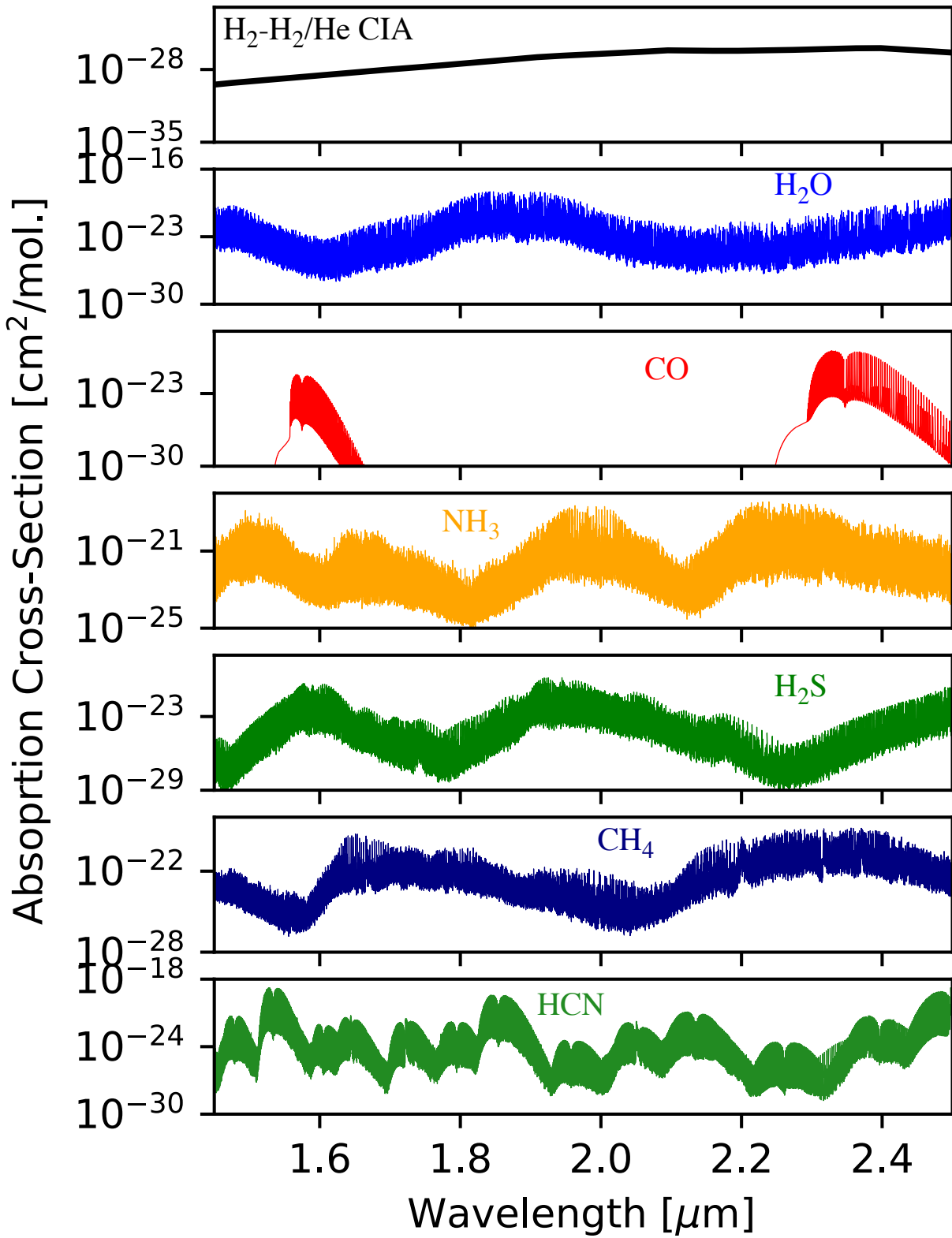
411 To bolster confidence in the isotopic ratio constraint, we perform a reverse injection and  
 412 retrieval test. To do this, we first perform a simplified retrieval (the 3-parameter TP-profile from  
 413 §4, H<sub>2</sub>O, CO, CO isotope ratio, the velocities, and stretch factor) on the data. We then reverse  
 414 inject (via division) the maximum likelihood spectrum (1+(F<sub>p</sub>/F<sub>\*</sub>), appropriately convolved and  
 415 Doppler shifted to each frame/phase) into the raw data sequence to remove the nominal planetary  
 416 signal<sup>9</sup>. Into this “best fit removed” data set we then re-inject the best fit model spectrum (through  
 417 multiplication) but with the <sup>13</sup>C<sup>16</sup>O abundance set to zero. We then re-retrieve on this model

418 injected dataset, resulting in only an upper limit on [ $^{13}\text{C}^{16}\text{O}/^{12}\text{C}^{16}\text{O}$ ], as expected (ED Fig. 6, top  
419 panels, black histograms). This suggests that there is real information in the data producing this  
420 constraint, that may not necessarily result in strong detection's in the classic sense.

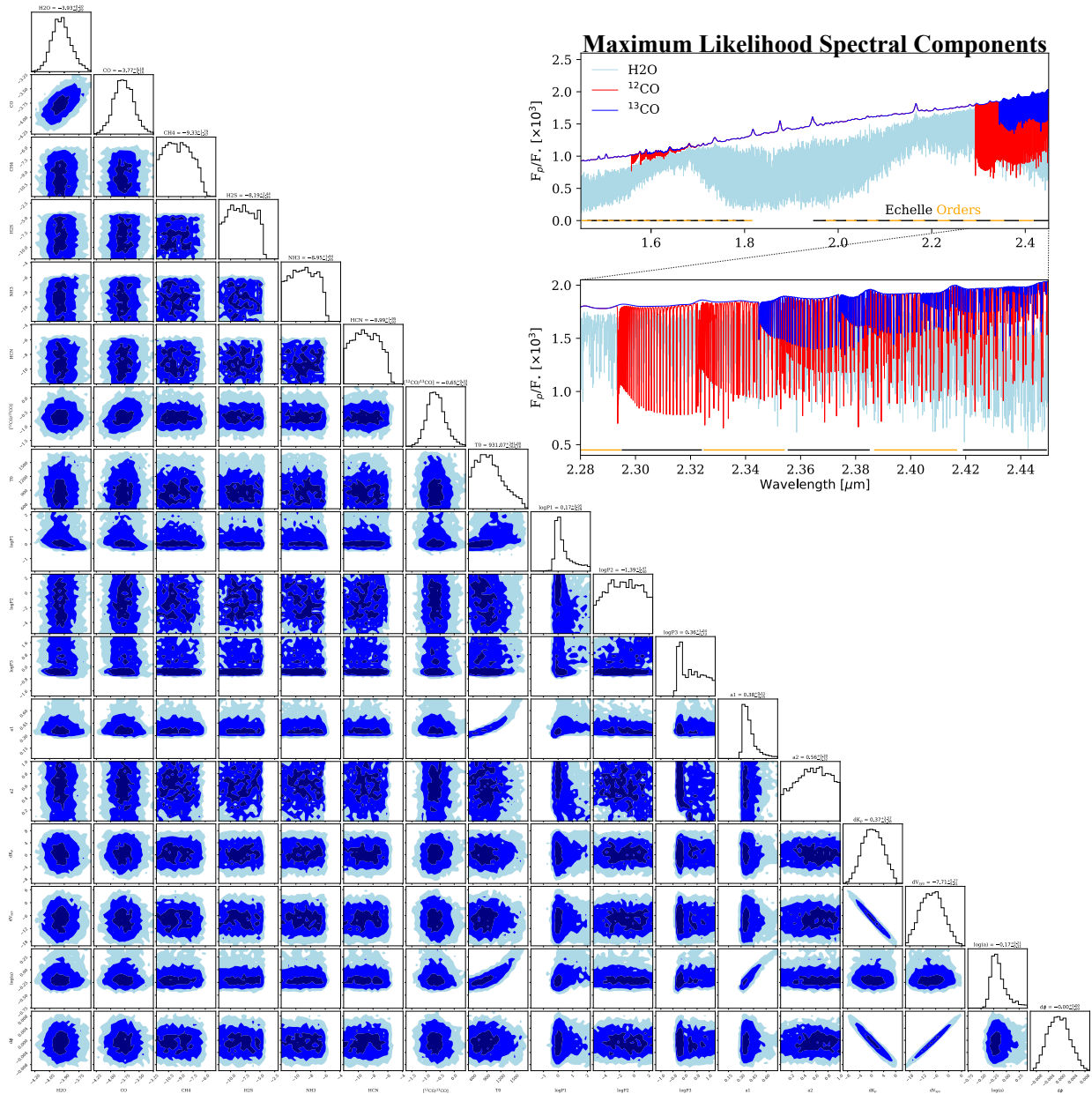
421 Finally, in ED Fig. 6, bottom panel, we compare the WASP-77Ab  $^{13}\text{C}/^{12}\text{C}$  constraint (via  
422 CO) to common solar system bodies and various reference values. It is currently beyond the scope  
423 of this manuscript to speculate as to why WASP-77Ab has a notably lower ratio than (enhanced  
424  $^{13}\text{C}$ ) compared to solar system, suffice it to say that protoplanetary disk chemistry models can  
425 produce a broad range of  $^{13}\text{C}/^{12}\text{C}$  in CO as a function of mid-plane height and radial distance  
426 from the star<sup>73</sup>. We purposefully choose not to strongly emphasize isotopic abundance constraint  
427 result in the main-text as more work needs to be done within the community to determine how  
428 to reliably quantify isotopic measurements—e.g., what is a detection?—this is non trivial for these  
429 types of observations<sup>75</sup>. Future observations are needed both for this planet and for others in order  
430 to determine the commonality of such constraints.



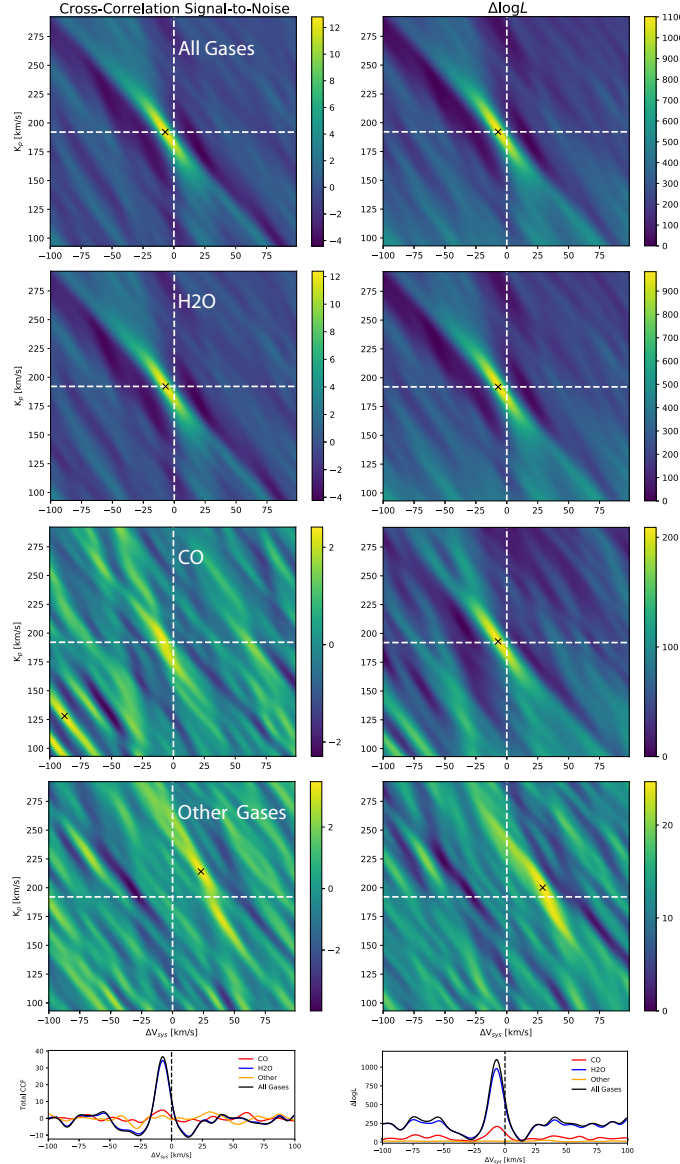
ED Fig. 1: Summary of the data and PCA procedure. a) shows the median per-resolution element signal-to-noise for each order for the night (in red). The blue curve is the median SNR in both time and over an individual order. b) shows example raw data cubes (top row)—spectra vs. time/frame for representative two orders (25, 5). Stationary tellurics show up as vertical dark streaks. Wavelength dependent gradient is due to the echelle blaze throughput. The PCA/SVD method can remove these stationary features, leaving behind the planetary signal buried in the noise (bottom row). We use these “Post-PCA” frames for the subsequent cross-correlation/retrieval analysis (repeated for all 43 use orders).



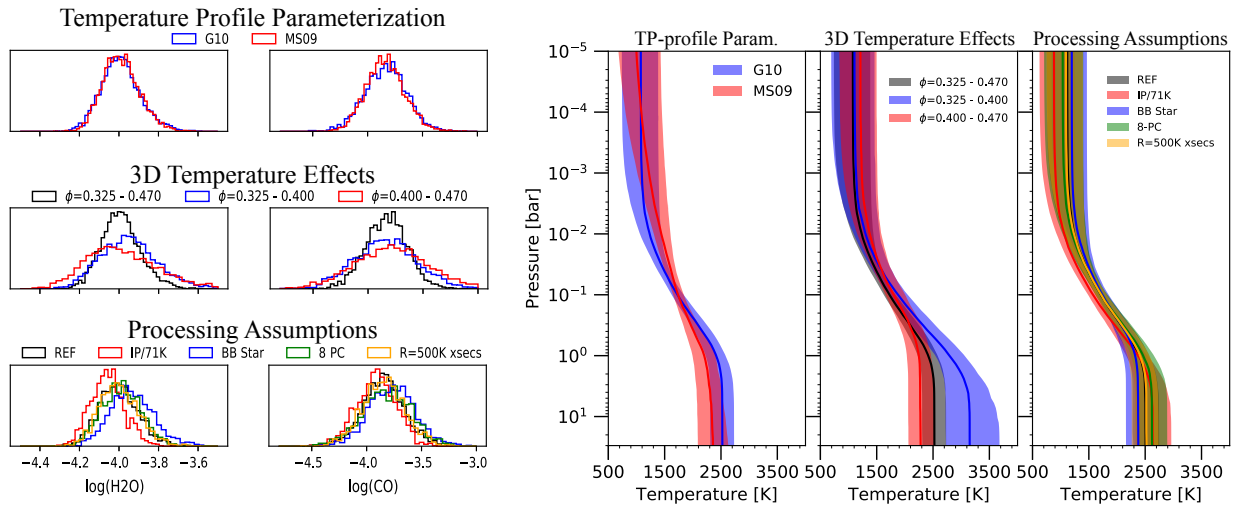
ED Fig. 2: Absorption cross-sections for the molecules considered in the retrieval analysis (for 0.01 bar, 1600K).



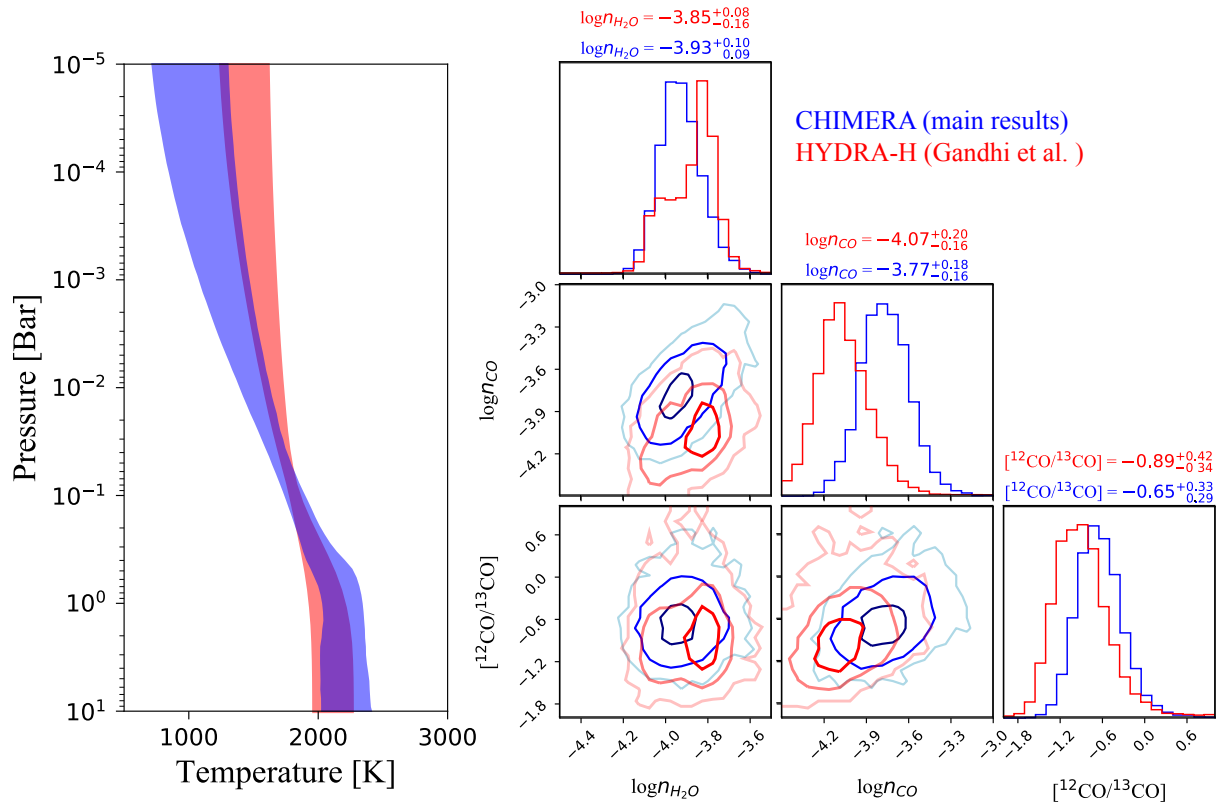
ED Fig. 3: Corner plot summary of the posterior probability distribution from the main-text retrieval analysis (the gases are in  $\log_{10}$  volume mixing ratio as in the main text). Note the bounded constraints on water, CO, and the isotopic ratio, but upper limits only on the other species. Note, we retrieve  $[^{13}\text{C}^{16}\text{O}/^{12}\text{C}^{16}\text{O}]$  but plot the inverse,  $[^{12}\text{C}^{16}\text{O}/^{13}\text{C}^{16}\text{O}]$  to facilitate comparisons to literature reported values (in ED Fig. 6) The inset shows the molecular components of the maximum likelihood model spectrum. Figure generated with `corner.py`



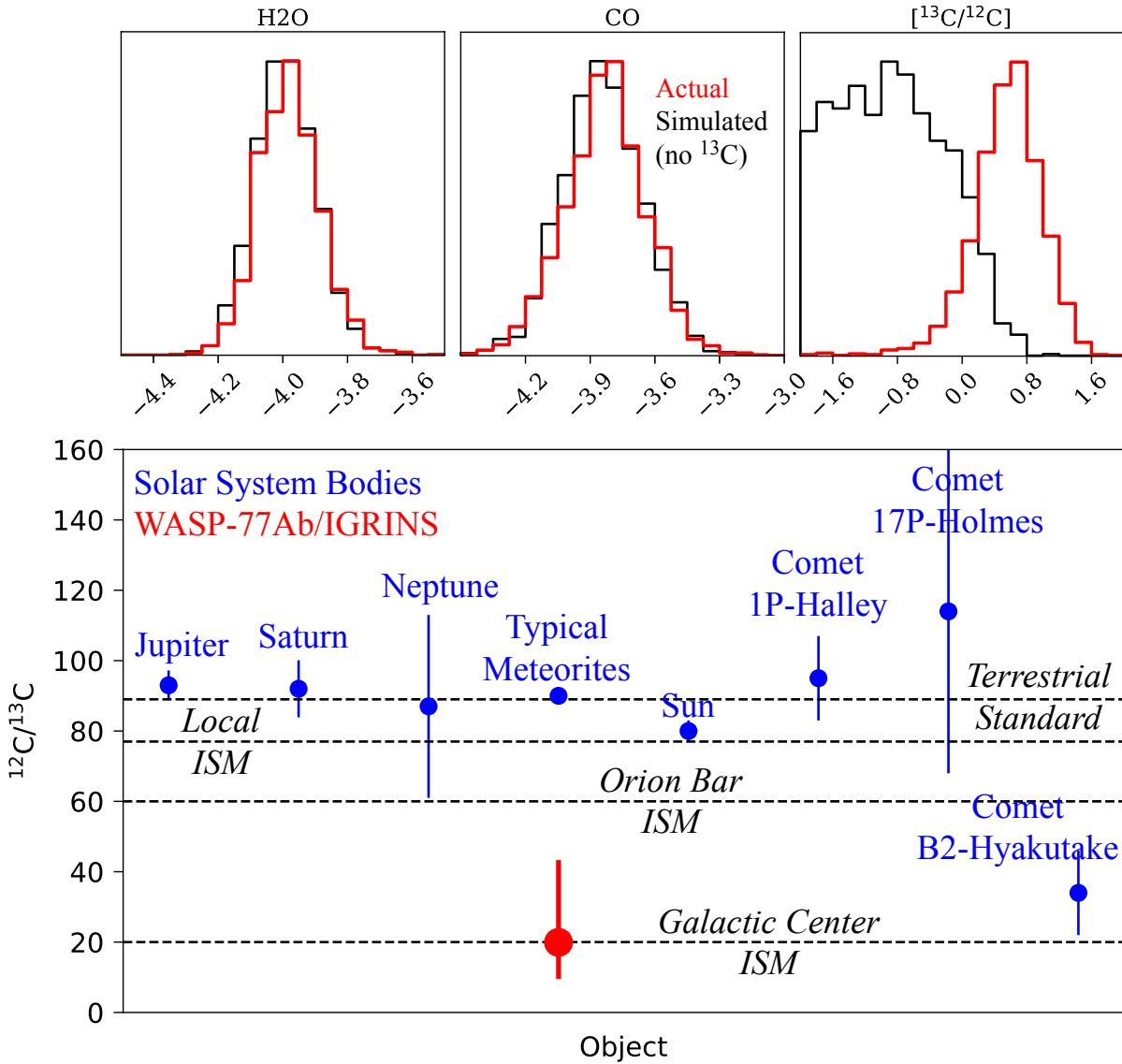
ED Fig. 4: Classic cross-correlation analysis data products (about the maximum likelihood solution/spectrum from the retrieval analysis). The left column illustrates the gas detection’s (all gases, H<sub>2</sub>O, CO, and other–NH<sub>3</sub>+H<sub>2</sub>S+HCN+CH<sub>4</sub>) in the standard  $K_p$ - $V_{sys}$  plane, with a slice in  $V_{sys}$  along the literature reported  $K_p$  at the bottom. The detection maps are constructed by subtracting the mean total CC, then dividing by an “off peak” (a boxed region in the lower left corner of each panel) CC standard deviation. Using this method, only H<sub>2</sub>O is strongly detected, with a hint of CO present at the expected velocities. The right column reproduces analogous products using the log-likelihood formalism<sup>14</sup> ( $\Delta\log L$  relative to the minimum), resulting in a stronger presence of CO. We emphasize, that while such maps may be instructive for “detecting” species or “atmosphere”, they do not marginalize over all of the degeneracy, nor do they maximize the information content in the data. This is why in our analysis, we focus on the the results arising from the more comprehensive log-likelihood/retrieval formalism.



ED Fig. 5: Robustness test analyses summary using the  $\text{H}_2\text{O}$ ,  $\text{CO}$ , and temperature profile constraints as the metrics for assumption impact. The top row of histograms and first TP-profile histogram demonstrate the lack of impact of TP-profile parameterization. The middle panel of histograms and middle TP-profile panel show that there is little impact due to any presence of temperature heterogeneities on the hemisphere(s) observed during the sequence. Finally, the bottom panel of histograms and last TP-profile panel illustrate the lack of impact of various data analysis and other minor modeling assumptions. In short, the retrieved abundances and temperature profile constraints are largely resilient against most common assumptions.



ED Fig. 6: Bayesian inference/retrieval tool comparison on the IGRINS data—CHIMERA (blue, primary tool used in this work) and HyDRA-H (red,<sup>18</sup>). The temperature profiles are compared in the left most panel and a subset of the abundances in the corner plot on the right. Each model uses slightly different atmospheric parameterization assumptions with the core radiative transfer aspects (solver, opacities) independently developed.



ED Fig. 7: Carbon isotopic abundance analysis. The top row of histograms compares the constraints from a nominal simplified retrieval model applied to the the true data (red) and an the reverse-injected data re-injected with <sup>13</sup>C isotope removed model (black). The upper limit on the simulated data and bounded constraint arising from the true dataset suggests that there is indeed isotopic information in these IGRINS data. The bottom panel compares the retrieved 12-C to 13-C ratio (red) to common solar system bodies (blue) and various reference values (black dashed lines). WASP-77Ab sits anomalously low (enhanced 13-C) compared to most solar system objects.

# References

1. Fortney, J. J., Dawson, R. I. & Komacek, T. D. Hot Jupiters: Origins, Structure, Atmospheres. *Journal of Geophysical Research (Planets)* **126**, e06629 (2021). 2102.05064.
2. Madhusudhan, N. Exoplanetary Atmospheres: Key Insights, Challenges, and Prospects. **57**, 617–663 (2019). 1904.03190.
3. Öberg, K. I., Murray-Clay, R. & Bergin, E. A. The Effects of Snowlines on C/O in Planetary Atmospheres. **743**, L16 (2011). 1110.5567.
4. Mordasini, C., van Boekel, R., Mollière, P., Henning, T. & Benneke, B. The Imprint of Exoplanet Formation History on Observable Present-day Spectra of Hot Jupiters. **832**, 41 (2016). 1609.03019.
5. Madhusudhan, N., Bitsch, B., Johansen, A. & Eriksson, L. Atmospheric signatures of giant exoplanet formation by pebble accretion. **469**, 4102–4115 (2017). 1611.03083.
6. Cridland, A. J., Pudritz, R. E. & Alessi, M. Composition of early planetary atmospheres - I. Connecting disc astrochemistry to the formation of planetary atmospheres. **461**, 3274–3295 (2016). 1605.09407.
7. Kreidberg, L. *et al.* Clouds in the atmosphere of the super-Earth exoplanet GJ1214b. **505**, 69–72 (2014). 1401.0022.
8. Wakeford, H. R. *et al.* The Complete Transmission Spectrum of WASP-39b with a Precise Water Constraint. **155**, 29 (2018). 1711.10529.
9. Pelletier, S. *et al.* Where is the Water? Jupiter-like C/H ratio but strong H<sub>2</sub>O depletion found on  $\tau$  Boötis b using SPIRou. *arXiv e-prints* arXiv:2105.10513 (2021). 2105.10513.
10. Maxted, P. F. L. *et al.* WASP-77 Ab: A Transiting Hot Jupiter Planet in a Wide Binary System. **125**, 48 (2013). 1211.6033.
11. Park, C. *et al.* Design and early performance of IGRINS (Immersion Grating Infrared Spectrometer). In Ramsay, S. K., McLean, I. S. & Takami, H. (eds.) *Ground-based and Airborne Instrumentation for Astronomy V*, vol. 9147 of *Society of Photo-Optical Instrumentation Engineers (SPIE) Conference Series*, 91471D (2014).
12. Mace, G. *et al.* IGRINS at the Discovery Channel Telescope and Gemini South. In Evans, C. J., Simard, L. & Takami, H. (eds.) *Ground-based and Airborne Instrumentation for Astronomy VII*, vol. 10702 of *Society of Photo-Optical Instrumentation Engineers (SPIE) Conference Series*, 107020Q (2018).
13. de Kok, R. J. *et al.* Detection of carbon monoxide in the high-resolution day-side spectrum of the exoplanet HD 189733b. **554**, A82 (2013). 1304.4014.

- 467 14. Brogi, M. & Line, M. R. Retrieving temperatures and abundances of exoplanet atmospheres  
468 with high-resolution cross-correlation spectroscopy. *AJ* **157**, 114 (2019).
- 469 15. Brogi, M. *et al.* The signature of orbital motion from the dayside of the planet  $\tau$  Boötis b.  
470 **486**, 502–504 (2012). 1206.6109.
- 471 16. Birkby, J. L. *et al.* Detection of water absorption in the day side atmosphere of HD 189733  
472 b using ground-based high-resolution spectroscopy at 3.2  $\mu\text{m}$ . **436**, L35–L39 (2013).  
473 1307.1133.
- 474 17. Snellen, I. A. G., de Kok, R. J., de Mooij, E. J. W. & Albrecht, S. The orbital motion,  
475 absolute mass and high-altitude winds of exoplanet HD209458b. **465**, 1049–1051 (2010).  
476 1006.4364.
- 477 18. Gandhi, S., Madhusudhan, N., Hawker, G. & Piette, A. HyDRA-H: Simultaneous Hybrid  
478 Retrieval of Exoplanetary Emission Spectra. **158**, 228 (2019). 1910.14042.
- 479 19. Moses, J. I. *et al.* Disequilibrium Carbon, Oxygen, and Nitrogen Chemistry in the Atmo-  
480 spheres of HD 189733b and HD 209458b. **737**, 15 (2011). 1102.0063.
- 481 20. Benneke, B. & Seager, S. How to Distinguish between Cloudy Mini-Neptunes and  
482 Water/Volatile-Dominated Super-Earths. *ArXiv e-prints* (2013). 1306.6325.
- 483 21. Feroz, F., Hobson, M. P. & Bridges, M. MULTINEST: an efficient and robust Bayesian infer-  
484 ence tool for cosmology and particle physics. **398**, 1601–1614 (2009). 0809.3437.
- 485 22. Giacobbe, P. *et al.* Five carbon- and nitrogen-bearing species in a hot giant planet’s atmo-  
486 sphere. **592**, 205–208 (2021). 2104.03352.
- 487 23. Hoeijmakers, H. J. *et al.* Atomic iron and titanium in the atmosphere of the exoplanet KELT-  
488 9b. **560**, 453–455 (2018). 1808.05653.
- 489 24. Parmentier, V., Fortney, J. J., Showman, A. P., Morley, C. & Marley, M. S. Transitions in the  
490 Cloud Composition of Hot Jupiters. **828**, 22 (2016). 1602.03088.
- 491 25. Asplund, M., Grevesse, N., Sauval, A. J. & Scott, P. The Chemical Composition of the Sun.  
492 **47**, 481–522 (2009). 0909.0948.
- 493 26. Madhusudhan, N., Amin, M. A. & Kennedy, G. M. Towards Chemical Constraints on Hot  
494 Jupiter Migration. *ArXiv e-prints* (2014). 1408.3668.
- 495 27. Booth, R. A., Clarke, C. J., Madhusudhan, N. & Ilee, J. D. Chemical enrichment of giant  
496 planets and discs due to pebble drift. **469**, 3994–4011 (2017). 1705.03305.
- 497 28. Welbanks, L. *et al.* Mass-Metallicity Trends in Transiting Exoplanets from Atmospheric  
498 Abundances of H<sub>2</sub>O, Na, and K. **887**, L20 (2019). 1912.04904.

- 499 29. Li, C. *et al.* The water abundance in Jupiter’s equatorial zone. *Nature Astronomy* **4**, 609–616  
500 (2020). 2012.10305.
- 501 30. Burrows, A. & Sharp, C. M. Chemical Equilibrium Abundances in Brown Dwarf and Extra-  
502 solar Giant Planet Atmospheres. **512**, 843–863 (1999). arXiv:astro-ph/9807055.
- 503 31. Atreya, S. K. *et al.* The Origin and Evolution of Saturn, with Exoplanet Perspective. *arXiv*  
504 *e-prints* arXiv:1606.04510 (2016). 1606.04510.
- 505 32. Thorngren, D. & Fortney, J. J. Connecting Giant Planet Atmosphere and Interior Modeling:  
506 Constraints on Atmospheric Metal Enrichment. **874**, L31 (2019). 1811.11859.
- 507 33. Lee, G., Dobbs-Dixon, I., Helling, C., Bognar, K. & Woitke, P. Dynamic mineral clouds on  
508 HD 189733b. I. 3D RHD with kinetic, non-equilibrium cloud formation. **594**, A48 (2016).  
509 1603.09098.
- 510 34. Piskorz, D. *et al.* Evidence for the Direct Detection of the Thermal Spectrum of the Non-  
511 Transiting Hot Gas Giant HD 88133 b. **832**, 131 (2016). 1609.09074.
- 512 35. Line, M. R. *et al.* A Systematic Retrieval Analysis of Secondary Eclipse Spectra. I. A Com-  
513 parison of Atmospheric Retrieval Techniques. **775**, 137 (2013). 1304.5561.
- 514 36. Line, M. R. *et al.* Uniform Atmospheric Retrieval Analysis of Ultracool Dwarfs. II. Properties  
515 of 11 T dwarfs. **848**, 83 (2017). 1612.02809.
- 516 37. Tennyson, J. *et al.* The 2020 release of the ExoMol database: molecular line lists for exoplanet  
517 and other hot atmospheres. *arXiv e-prints* arXiv:2007.13022 (2020). 2007.13022.
- 518 38. Rothman, L. S. *et al.* HITEMP, the high-temperature molecular spectroscopic database. **111**,  
519 2139–2150 (2010).
- 520 39. Hargreaves, R. J. *et al.* An Accurate, Extensive, and Practical Line List of Methane for the  
521 HITEMP Database. **247**, 55 (2020). 2001.05037.
- 522 40. Li, G. *et al.* Rovibrational Line Lists for Nine Isotopologues of the CO Molecule in the X  $^1\Sigma^+$   
523 Ground Electronic State. **216**, 15 (2015).
- 524 41. Azzam, A. A. A., Tennyson, J., Yurchenko, S. N. & Naumenko, O. V. ExoMol molecu-  
525 lar line lists - XVI. The rotation-vibration spectrum of hot H<sub>2</sub>S. **460**, 4063–4074 (2016).  
526 1607.00499.
- 527 42. Barber, R. J. *et al.* ExoMol line lists - III. An improved hot rotation-vibration line list for HCN  
528 and HNC. **437**, 1828–1835 (2014). 1311.1328.
- 529 43. Karman, T. *et al.* Update of the HITRAN collision-induced absorption section. **328**, 160–175  
530 (2019).

- 531 44. Grimm, S. L. & Heng, K. HELIOS-K: An Ultrafast, Open-source Opacity Calculator for  
532 Radiative Transfer. **808**, 182 (2015). 1503.03806.
- 533 45. Grimm, S. L. *et al.* HELIOS-K 2.0 Opacity Calculator and Open-source Opacity Database for  
534 Exoplanetary Atmospheres. **253**, 30 (2021). 2101.02005.
- 535 46. Polyansky, O. L. *et al.* ExoMol molecular line lists XXX: a complete high-accuracy line list  
536 for water. **480**, 2597–2608 (2018). 1807.04529.
- 537 47. Gharib-Nezhad, E. *et al.* EXOPLINES: Molecular Absorption Cross-Section Database for  
538 Brown Dwarf and Giant Exoplanet Atmospheres. *arXiv e-prints* arXiv:2104.00264 (2021).  
539 2104.00264.
- 540 48. Madhusudhan, N. & Seager, S. A Temperature and Abundance Retrieval Method for Exo-  
541 planet Atmospheres. **707**, 24–39 (2009). 0910.1347.
- 542 49. Buchner, J. *et al.* X-ray spectral modelling of the AGN obscuring region in the CDFS:  
543 Bayesian model selection and catalogue. **564**, A125 (2014). 1402.0004.
- 544 50. Line, M. R., Knutson, H., Deming, D., Wilkins, A. & Desert, J.-M. A Near-infrared Trans-  
545 mission Spectrum for the Warm Saturn HAT-P-12b. **778**, 183 (2013). 1310.4796.
- 546 51. Line, M. R., Knutson, H., Wolf, A. S. & Yung, Y. L. A Systematic Retrieval Analysis of  
547 Secondary Eclipse Spectra. II. A Uniform Analysis of Nine Planets and their C to O Ratios.  
548 **783**, 70 (2014). 1309.6663.
- 549 52. Trotta, R. Bayes in the sky: Bayesian inference and model selection in cosmology. *Contem-  
550 porary Physics* **49**, 71–104 (2008). 0803.4089.
- 551 53. Benneke, B. & Seager, S. Atmospheric Retrieval for Super-Earths: Uniquely Constraining the  
552 Atmospheric Composition with Transmission Spectroscopy. **753**, 100 (2012). 1203.4018.
- 553 54. Brogi, M. *et al.* Detection of Molecular Absorption in the Dayside of Exoplanet 51 Pegasi b?  
554 **767**, 27 (2013). 1302.6242.
- 555 55. Beltz, H., Rauscher, E., Brogi, M. & Kempton, E. M. R. A Significant Increase in Detection  
556 of High-resolution Emission Spectra Using a Three-dimensional Atmospheric Model of a Hot  
557 Jupiter. **161**, 1 (2021). 2009.09030.
- 558 56. Piskorz, D. *et al.* Ground- and Space-based Detection of the Thermal Emission Spectrum of  
559 the Transiting Hot Jupiter KELT-2Ab. **156**, 133 (2018). 1809.05615.
- 560 57. Gharib-Nezhad, E. & Line, M. R. The Influence of H<sub>2</sub>O Pressure Broadening in High-  
561 metallicity Exoplanet Atmospheres. **872**, 27 (2019). 1809.02548.
- 562 58. Arcangeli, J. *et al.* H<sup>-</sup> Opacity and Water Dissociation in the Dayside Atmosphere of the Very  
563 Hot Gas Giant WASP-18b. **855**, L30 (2018). 1801.02489.

- 564 59. Mansfield, M. *et al.* An HST/WFC3 Thermal Emission Spectrum of the Hot Jupiter HAT-P-7b.  
565 **156**, 10 (2018). 1805.00424.
- 566 60. Tsai, S.-M. *et al.* Toward Consistent Modeling of Atmospheric Chemistry and Dynamics  
567 in Exoplanets: Validation and Generalization of the Chemical Relaxation Method. **862**, 31  
568 (2018). 1711.08492.
- 569 61. Fortney, J. J., Lodders, K., Marley, M. S. & Freedman, R. S. A Unified Theory for the  
570 Atmospheres of the Hot and Very Hot Jupiters: Two Classes of Irradiated Atmospheres. **678**,  
571 1419–1435 (2008). 0710.2558.
- 572 62. Perez-Becker, D. & Chiang, E. Catastrophic evaporation of rocky planets. **433**, 2294–2309  
573 (2013). 1302.2147.
- 574 63. Parmentier, V., Showman, A. P. & Fortney, J. J. The cloudy shape of hot Jupiter thermal phase  
575 curves. **501**, 78–108 (2021). 2010.06934.
- 576 64. Burrows, A., Sudarsky, D. & Hubeny, I. Theory for the Secondary Eclipse Fluxes, Spectra,  
577 Atmospheres, and Light Curves of Transiting Extrasolar Giant Planets. **650**, 1140–1149  
578 (2006). arXiv:astro-ph/0607014.
- 579 65. Atreya, S. K. *et al.* The Origin and Evolution of Saturn, with Exoplanet Perspective. *arXiv*  
580 *e-prints* arXiv:1606.04510 (2016). 1606.04510.
- 581 66. Fortney, J. J. *et al.* A Framework for Characterizing the Atmospheres of Low-Mass Low-  
582 Density Transiting Planets. *ArXiv e-prints* (2013). 1306.4329.
- 583 67. Pinhas, A., Madhusudhan, N., Gandhi, S. & MacDonald, R. H<sub>2</sub>O abundances and cloud  
584 properties in ten hot giant exoplanets. **482**, 1485–1498 (2019). 1811.00011.
- 585 68. Fisher, C. & Heng, K. Retrieval analysis of 38 WFC3 transmission spectra and resolution of  
586 the normalization degeneracy. **481**, 4698–4727 (2018). 1809.06894.
- 587 69. Guillot, T. & Havel, M. An analysis of the CoRoT-2 system: a young spotted star and its  
588 inflated giant planet. **527**, A20 (2011). 1010.1078.
- 589 70. Line, M. R. *et al.* Information Content of Exoplanetary Transit Spectra: An Initial Look. **749**,  
590 93 (2012). 1111.2612.
- 591 71. Feng, Y. K. *et al.* The Impact of Non-uniform Thermal Structure on the Interpretation of  
592 Exoplanet Emission Spectra. **829**, 52 (2016). 1607.03230.
- 593 72. Gandhi, S. *et al.* Molecular cross-sections for high-resolution spectroscopy of super-Earths,  
594 warm Neptunes, and hot Jupiters. **495**, 224–237 (2020). 2004.04160.
- 595 73. Woods, P. M. & Willacy, K. Carbon Isotope Fractionation in Protoplanetary Disks. **693**,  
596 1360–1378 (2009). 0812.0269.

- 597 74. Marboeuf, U., Thiabaud, A., Alibert, Y. & Benz, W. Isotopic ratios D/H and  $^{15}\text{N}/^{14}\text{N}$  in giant  
598 planets. **475**, 2355–2362 (2018).
- 599 75. Mollière, P. & Snellen, I. A. G. Detecting isotopologues in exoplanet atmospheres using  
600 ground-based high-dispersion spectroscopy. **622**, A139 (2019). 1809.01156.